Inorganica Chimica Acta 430 (2015) 132–143

Contents lists available at ScienceDirect

Inorganica Chimica Acta

journal homepage: www.elsevier.com/locate/ica

# Computational and spectroscopic characterization of key intermediates of the Selective Catalytic Reduction cycle of NO on zeolite-supported Cu catalyst

Douglas W. Crandell [a], Haiyang Zhu [b], Xiaofan Yang [b,*], John Hochmuth [b], Mu-Hyun Baik [a,c,*]

[a] Department of Chemistry, Indiana University, 800 E. Kirkwood Avenue, Bloomington, IN 47405, USA
[b] BASF Corporation, 25 Middlesex/Essex Turnpike, Iselin, NJ 08830, USA
[c] Department of Materials Chemistry, Korea University, Jochiwon-eup, Sejong-si, 339-700, South Korea

ARTICLE INFO

*Article history:*
Received 17 February 2015
Accepted 19 February 2015
Available online 2 March 2015

*Keywords:*
Selective Catalytic Reduction
Zeolite
DRIFT
DFT

ABSTRACT

Chabazite supported Cu is a promising catalyst platform for implementing a $NH_3$/urea-based Selective Catalytic Reduction (SCR) system to remove hazardous $NO_x$ gases from lean-burn engine exhaust. Whereas in-depth spectroscopic and other studies have attempted to identify key features of the catalytic cycle previously, a deep understanding of the SCR mechanism amenable to systematic improvement of catalyst performance remains elusive. For example, neither the precise Cu coordination geometry at the active site nor the substrate binding affinities to the catalytic center are known. To establish a more rational approach to catalyst optimization based on the thermodynamics and kinetics of the key steps of the underlying $NO_x$-transformations we developed a quantum chemical model and benchmarked it to match vibrational data from Diffuse Reflectance Infrared Fourier Transform spectroscopy resulting in plausible assignments of each observable intermediate to specific oxidation states of Cu and NO-binding properties. Among these intermediates, we identified the structure of a lattice supported $NO^+$ cation species, expected to be reactive towards $NH_3$, corresponding to a high frequency IR-absorption at 2170 $cm^{-1}$. This approach enables a more precise assignment of the experimental vibrational data to key intermediates potentially involved in the catalytic cycle in order to develop a micromechanistic proposal for the catalysis that is chemically meaningful and is logically consistent.



## 1. Introduction

$NH_3$/urea driven Selective Catalytic Reduction (SCR) is a leading technology for eliminating hazardous $NO_x$ gases ($NO + NO_2$) in lean-burn engine exhaust [1–4]. Under standard SCR conditions NO is reduced by ammonia in the presence of excess amounts of $O_2$ to give $N_2$ and water vapor, i.e. $4NO + 4NH_3 + O_2 \rightarrow 4N_2 + 6H_2O$. To promote the necessary coupling between NO and $NH_3$ and consume unused $NH_3$ a catalytic platform is required [5]. Currently, the most widely used SCR catalyst systems can be divided in two major categories: metal oxides, represented for example by $V_2O_5$ [6–9], and zeolite supported transition metals [10–13]. The latter show a wider operation temperature window and higher $NO_x$ conversion efficiency at low temperatures [14]. The most promising among the zeolite/metal systems is the chabazite (CHA) supported Cu catalyst, specifically Cu-SSZ-13, which was patented by BASF several years ago [15]. A series of studies have been conducted recently using both experimental [16–25] and computational [26–31] techniques to shed light on the inner workings of Cu-SSZ-13, and it is now accepted that the active site is a single Cu atom hosted by a six-membered ring of the double six-membered ring (d6R) building unit in the SSZ-13 zeolite [32]. Although previous computer models have successfully reproduced the coordination number and bond lengths [29–31] of Cu-SSZ-13 that was determined experimentally by EXAFS [16], no consensus mechanism has emerged for the SCR reaction promoted by Cu-SSZ-13. This lack of fundamental understanding of how the NO reduction is catalyzed frustrating and makes it difficult to devise rational design and optimization strategies for new high-performance catalysts.

Among the desired improvements in the next generation catalysts, the most urgently needed is significantly enhanced low temperature reactivity at 150–200 °C [33]. Since there is no understanding of the SCR reaction mechanism at an atomic detail,

* Corresponding authors.
*E-mail addresses:* xiaofan.yang@basf.com (X. Yang), mbaik@indiana.edu (M.-H. Baik).

http://dx.doi.org/10.1016/j.ica.2015.02.021
0020-1693/

currently employed optimization schemes are neither rationally conceived nor guided by a conceptual plan. Instead, empirical and somewhat arbitrary explorations of catalyst discovery are conducted that are both time-consuming and costly. For instance, it was found that tuning the Cu content in Cu-SSZ-13 can lead to higher performance of the catalytic system at low temperature, but that enhancement came at the cost of losing the reactivity at high temperature conditions [34] – the relationship between Cu-content and chemical reactivity and high/low temperature conditions is not well understood.

In order to develop new ideas and build a foundation for more rational, mechanism-based strategies of catalyst optimization, we must obtain a better understanding of the catalytic mechanism. Specifically, we must: (1) strengthen the know-how about the atomistic NO-binding and NO-processing properties of Cu-SSZ-13; (2) identify the rate-determining step in the catalytic cycle to de-bottleneck the low temperature performance on Cu-SSZ-13; (3) devise logical catalyst design strategies that identify clear goals for catalyst composition and, (4) formulate precise descriptions of all key reaction steps in the SCR process promoted by Cu-SSZ-13. The foundation for accomplishing these goals is a detailed, atomistic level knowledge about the identity of the key intermediate species involved in the catalysis.

Quantum chemical molecular modeling is an attractive method of inquiry that can provide insights about the catalytic mechanism at a sufficiently high resolution to answer some of the aforementioned questions [35]. Structures and energies of intermediates and transition states encountered in the catalytic cycle can be computed precisely and evaluated against alternative reaction trajectories [36–38]. Recent advances in computational hardware and software allow for constructing computer models that are realistic in size and that are sufficiently sophisticated, such that direct comparisons to experimental observations, such as intermediate structures and vibrational frequencies, can be made to benchmark and refine the computer model. In particular, Density Functional Theory (DFT) [39,40] emerged as the method of choice for complex reaction modeling studies. Previous experimental work [16] based on EXAFS provided important details about the coordination environment of Cu in Cu-SSZ-13. In this work, we combine Diffuse Reflectance Infrared Fourier Transform spectroscopic (DRIFTs) [41–43] data and quantum chemical molecular modeling studies. Vibrational spectra of intermediate species formed by NO binding to the Cu sites in Cu-SSZ-13 and undergoing reductions are acquired and analyzed. DFT-based molecular models are employed to explicitly consider various Cu–NO binding motifs and chemical transformations that may take place. The characteristic Cu–NO vibrational frequencies from DRIFTs measurements are used in addition to computed energies and electronic structure patterns to correlate computed intermediate structures to experiments. In doing so, we are able to not only assign and explain the changes in the vibrational spectra obtained during the reaction of Cu-SSZ-13 with NO, but also construct important portions of the catalytic cycle and rationally propose intermediates that may or may not be observable experimentally. This work constitutes the first step towards building the foundation for a more detailed study that will construct a complete catalytic reaction mechanism and identify the rate-determining step with the specific aim to improve the low temperature SCR performance.

## 2. Technical details

### 2.1. Experimental

Cu-SSZ-13 (SAR @ 25 and Cu% = 2.2%), with high crystallinity and small amounts of CuO, has been chosen for the DRIFTs study. NO adsorption measurements were taken on a Bio-Rad Excalibur FTS 3000 IR spectrometer equipped with a MCT detector and a Harrick high-temperature environmental chamber with ZnSe windows. The samples were ground into fine powder and filled into the sample cup. The sample powders were first dehydrated at 400 °C for 1 h in a flowing stream of Ar at a rate of 40 mL/min, and then cooled down to 30 °C. A spectrum was taken for the sample prior to the adsorption of probe molecule (e.g., NO) as the background. 1% of NO in Ar was introduced into the chamber. The spectra were sampled at NO exposure time of 0.5, 2, 5, 10, 15, 20, and 30 min. Differential spectra were obtained by subtracting the background spectrum without NO adsorption from the spectrum saturated with NO. For NO adsorption on reduced samples, the same sample was used in the NO adsorption test. The samples were reduced by 3% of $H_2$ in Ar at 400 °C for 1 h and then cooled down to 30 °C. The samples were purged by Ar at a flow rate of 40 mL/min for 10 min. A spectrum was taken for the sample prior to probe molecule adsorption as the background. The NO adsorption process was repeated as described above.

### 2.2. Computational

Cluster model calculations were carried out using Density Functional Theory [39,40] as implemented in the Jaguar 8.1 suite of *ab initio* quantum chemistry programs [44]. Geometry optimizations were performed at the PBE/6-31G** level of theory [45,46] with copper represented by the Los Alamos LACVP basis set [47,48], which includes relativistic effective core potentials. More reliable single point energies were computed from the optimized geometries using Dunning's correlation-consistent triple-ζ basis set, cc-pVTZ(-f) [49], where copper was represented using a modified version of LACVP, designated as LACV3P with decontracted exponents to match the effective core potential with a triple-ζ quality basis. Vibrational frequency analysis was performed at the PBE/6-31G** level of theory to derive zero point energy and vibrational entropy corrections from unscaled frequencies. To correlate computed vibrational frequencies with experiments, scaling factors (0.961 for B3LYP and 0.989 for PBE) were used from the Computational Chemistry Comparison and Benchmark Database [50].

The energy components have been computed with the following protocol. The free energy in gas phase $G(\text{gas})$ has been calculated as follows:

$$G(\text{gas}) = H(\text{gas}) - TS(\text{gas}) \quad (1)$$

$$H(\text{gas}) = E(\text{SCF}) + \text{ZPE} \quad (2)$$

$$\Delta G(\text{gas}) = \sum G(\text{gas}) \text{ for products} - \sum G(\text{gas}) \text{ for reactants} \quad (3)$$

$G(\text{gas})$ is the free energy in gas phase; $H(\text{gas})$ is the enthalpy in gas phase; $T$ is the temperature (298 K); $S(\text{gas})$ is the entropy in gas phase; $E(\text{SCF})$ is the self-consistent field energy, i.e. "raw" electronic energy as computed from the SCF procedure and *ZPE* is the zero point energy.

To calculate the crystal models, the Vienna *ab initio* simulation package (VASP) [51,52] was used. Kohn–Sham equations of DFT were solved within a plane-wave basis set and using periodic boundary conditions. The projector augmented wave (PAW) method developed by Blöchl [53] and modified by Kresse and Joubert [54] was used to represent the electron–ion interaction. Calculations were performed with the PBE [45] functional and use PAW potentials constructed using core wave-functions calculated with the PBE functional. All calculations were performed in a spin-polarized mode to accurately describe different spin-states of the extra-framework cations and of paramagnetic adsorbates

including NO. To accurately describe the oxygen orbitals and the eigenstates of the extra-framework cations, a plane-wave energy cutoff of 400 eV was used. During self-consistency iterations and for the calculation of the Hellmann–Feynman forces acting on the atoms Brillouin-zone sampling was restricted to the Γ-point, which is justifiable for the large unit cell size of chabazite [29]. Geometry optimizations at constant volume were performed using a mixture of damped molecular dynamics, conjugate gradient, and quasi-Newton algorithms as implemented in VASP, using analytical Hellmann–Feynman forces. The initial volume was determined by allowing the cell shape and internal coordinates to relax independently. Convergence was assumed when the forces on the atoms were smaller than 0.05 eV $Å^{-1}$.

Coupled-cluster calculations for the overall thermodynamics of the catalytic cycle with singles, doubles, and perturbative triples (CCSD(T)) [55] were performed using the ORCA quantum chemistry package [56] and using Dunning's correlation-consistent cc-pVTZ and cc-pVQZ basis sets [49].

## 3. Results and discussions

Designing a chemical computer model that can deliver helpful answers to specific questions requires that several important decisions are made about the conceptual and technical details of the model. Using periodic boundary conditions that will replicate a small, explicitly treated molecular unit *ad infinitum*, we can approximate the periodically repetitive nature of crystalline materials. Whereas such models are appropriate for studying bulk properties, so-called cluster models that contain the chemically most relevant portion of the larger assembly as a molecular entity can also provide important insight. In this work we use both modeling approaches to construct a unified model and exploit the advantages of each method while avoiding their known limitations.

### 3.1. Aluminate distribution

Before our computer models can be used to interpret the DRIFTs experiments and investigate the mechanism of SCR, several preliminary investigations were necessary to validate the computational methodology and to propose precise structures of the molecular species suspected to be present during the catalytic cycle, for which experimental structures are not available. First, we examined several potential structures of the Al-doped CHA-zeolite [57] and determined the preferred Cu(I)/Cu(II) binding environment based on the computed energies from our periodic solid state models to provide suitable starting geometries for the following investigations. The SCR reaction between NO and $NH_3$ is thought to proceed through a redox mechanism that samples Cu(I)/Cu(II) [20,26]. Chabazite is an ideal platform for computational modeling studies, as the 36 tetrahedral centers within the unit-cell are symmetry equivalent. As illustrated in Fig. 1, the unit cell of the chabazite can be envisioned to consist of two connected constructs, each containing two silicate-based six-membered rings that are stacked on top each other. One of the six-membered rings on each sub-unit is decorated with 6 other silicate units that will be used to connect to the neighboring cell. Fig. 1 illustrates the 9 positions within the unit-cell of the zeolite that we considered as potential substitution sites of the aluminum dopant. We found that there is no meaningful energetic preference for the 9 positions with the exception of position **E**, which gives a slightly higher energy of ~3.5 kcal $mol^{-1}$ than the other substitution sites.

Adding a second aluminum ion into the zeolite structure, five possible isomers can be envisioned, as illustrated in Fig. 2. The energies of these systems were determined using both a small cluster (d6R unit) and the periodic crystal models. Interestingly, the cluster model prefers structure **2Al-4**, where one Al ion is placed on each of the six-membered rings, as to maximize the separation of the two Al-substituted sites and minimize the electrostatic repulsion between the two formally negatively charged $AlO_4$-fragments. Our periodic crystal model estimates the energy difference between the different structural isomers to be much smaller, suggesting that within a solid where charges can be dissipated over a larger fragment of the crystal, the individual electrostatic interactions between the aluminate fragments are not as distinctive as seen in a cluster model.

Electrostatic interactions play an important role in determining where the copper ion is located. Fig. 3 summarizes five different positions for Cu(I) that were tested in our computer simulations. Our periodic crystal model predicts that structure **AlCu(I)-1**, where the copper cation is placed at the center of the 6-membered ring that contains the Al ion is most favorable energetically. Experimental results have also previously shown that the center of a 6-membered ring is the most favorable binding position for the Cu ion [16,17,58]. Although, a recent study by Peden and coworkers has shown that 8-membered rings may also potentially be active for the SCR of NO with $NH_3$ [59]. Placing the Cu(I) ion at the corresponding central position of the second six-membered ring that does not contain the Al-ion gives rise to structure **AlCu(I)-2**, which is 13.5 kcal $mol^{-1}$ higher in energy than **AlCu(I)-1**. The

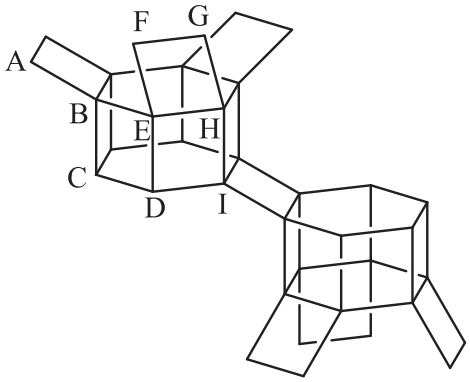


| Al Position | A | B | C | D | E | F | G | H | I |
|---|---|---|---|---|---|---|---|---|---|
| $E_{relative}$ (kcal $mol^{-1}$) | 0.00 | 0.29 | 0.19 | 0.52 | 3.46 | 0.16 | 0.62 | 0.25 | 0.51 |

**Fig. 1.** Selected positions for 1-Al substitution within the repeating cell of CHA and relative energies estimated by periodic crystal model.

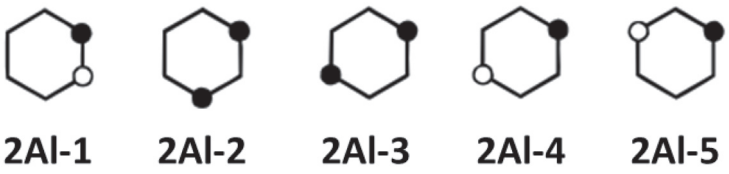


| Al Position | 2Al-1 | 2Al-2 | 2Al-3 | 2Al-4 | 2Al-5 |
|---|---|---|---|---|---|
| $E_{relative}$ (cluster) | 1.68 | 5.99 | 6.15 | 0.00 | 3.02 |
| $E_{relative}$ (crystal) | 0.00 | 2.18 | 0.94 | 2.31 | 3.15 |

**Fig. 2.** Possible configurations for 2-Al substitution in CHA framework and relative energies in kcal mol$^{-1}$ (solid circle represents the Al on top six-member ring and open circle stands for the Al on the bottom six-member ring of the d6R unit).

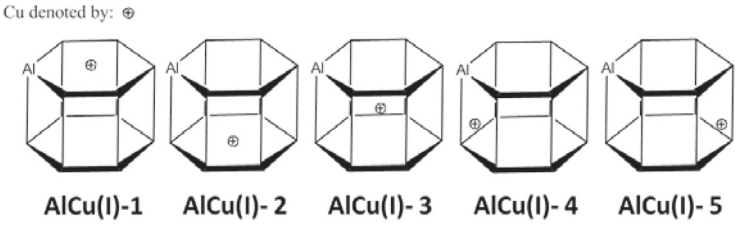


| Al-Cu Config | AlCu(I)-1 | AlCu(I)-2 | AlCu(I)-3 | AlCu(I)-4 | AlCu(I)-5 |
|---|---|---|---|---|---|
| $E_{relative}$(cluster) | 0.00 | 12.04 | →AlCu(I)-1 | 31.20 | 34.80 |
| $E_{relative}$(crystal) | 0.00 | 13.53 | →AlCu(I)-1 | 15.58 | →AlCu(I)-1 |

**Fig. 3.** Possible Cu(I) binding sites evaluated using the periodic crystal model. Relative energies are given in kcal mol$^{-1}$.

putative copper binding modes **AlCu(I)-3** and **AlCu(I)-5** are not proper, as they do not represent local minima on the potential energy surface.Cu(I) ions placed in these positions move during geometry optimization to converge to structure **AlCu(I)-1**. Whereas it is plausible that **AlCu(I)-1** is the lowest energy geometry, as it allows for the negative partial charge of the $[AlO_4]^-$ fragment to interact favorably with the positive partial charge of the Cu(I) cation, it is interesting that the energies of the other isomers are within ~15 kcal mol$^{-1}$. This modest energy difference suggests that from a thermodynamic standpoint, Cu(I) may display a much higher mobility within the zeolite framework than anticipated. The relatively high operational temperature of the Cu-SSZ-13 system makes this point particularly relevant.

The relative energies of Cu(II)-binding show similar trends to those of Cu(I)-binding – the absolute energies are intuitively much larger due to the increased electrostatic attraction between the dicationic copper center and the zeolite framework. The computed energies are summarized in Fig. 4. Cu(II) prefers to stay within the six-member ring that contains the aluminate dopant and **AlCu(II)-1** is the energetically preferred geometry. Structure **AlCu(II)-3**, where the Cu(II) ion is placed in the spatial center of the bicyclic unit, is again not a minimum and the geometry converges to the **AlCu(II)-1** structure. Compared to this lowest energy structure, the other possible minima are ~35 kcal mol$^{-1}$ higher in energy, suggesting that these isomers should be out of reach even at elevated temperatures.

Scenarios of Cu(II) supported by CHA carrying two aluminate-substituents are also explored, as a typical Si/Al ratio of 15 found in CHA suggests that there should be an average of two Al atoms per unit cell [57]. The Al atoms are positioned diagonally within the same six-member rings to minimize the electrostatic repulsion. The five possible Cu(II) locations are shown in Fig. 5. The most preferred configuration was identified again as **$Al_2$Cu(II)-1**, where Cu(II) is positioned at the center of the six-member ring. As seen for the Cu(I) binding, structure **$Al_2$Cu(II)-3** is not a valid minimum and converges to structure **$Al_2$Cu(II)-1**.

Fig. 6 compares the optimized structures of the most preferred binding sites for Cu(I)/Cu(II) with optional Al support sites. In general, without the rigid framework imposed by the zeolite, cluster model tends to produce more compact structures with higher coordination numbers around Cu. The cluster models give familiar trigonal planar coordination geometries for the Cu(I) center, whereas the periodic crystal models predict slightly distorted geometries. The Cu(II) models both give distorted square planar geometries with Cu forming shorter bonds to the framework oxygen atoms bound to aluminum.

### 3.2. DRIFTs of Cu-SSZ-13

Fig. 7a shows the NO-stretching regions of the IR-absorption spectra collected at different NO exposure times on dehydrated Cu-SSZ-13 in Ar. At $t$ = 0.5 min (black line in Fig. 7), the dominating feature is a relatively sharp band at 1810 cm$^{-1}$, which is assigned to the N–O stretching mode of a Cu(I)–NO species. Upon increasing the NO exposure time, the 1810 cm$^{-1}$ band decreases quickly within the first 10 min. Interestingly, there appears to be a transiently enriched species **X1** with a vibrational mode at 1946 cm$^{-1}$ that rises in population in the first 10 min and vanishes, as new bands associated with the NO-reduction products appear. The higher frequency N–O stretching mode indicates that the

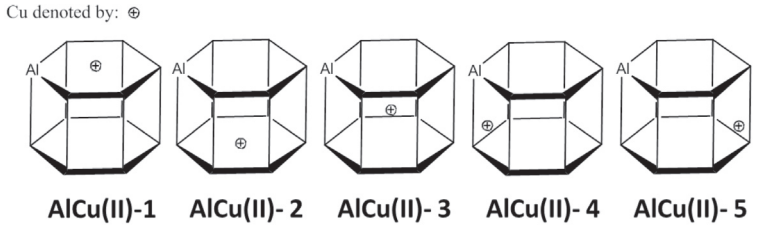


| Al-Cu(II) Config | AlCu(II)-1 | AlCu(II)-2 | AlCu(II)-3 | AlCu(II)-4 | AlCu(II)-5 |
|---|---|---|---|---|---|
| $E_{relative}$ (cluster) | 0.00 | 36.34 | →**AlCu(II)-1** | 33.85 | 55.04 |
| $E_{relative}$ (crystal) | 0.00 | 22.91 | →**AlCu(II)-1** | 26.51 | 32.45 |

**Fig. 4.** Possible Cu(II) binding locations (with 1-Al support) and relative energies estimated by cluster model in kcal mol$^{-1}$. All structures were modeled as cations.

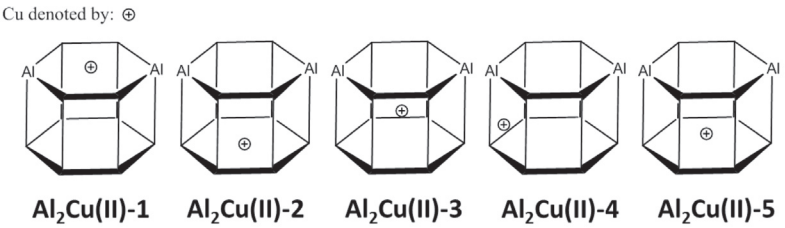


| 2Al-Cu(II) Config | $Al_2Cu(II)$-1 | $Al_2Cu(II)$-2 | $Al_2Cu(II)$-3 | $Al_2Cu(II)$-4 | $Al_2Cu(II)$-5 |
|---|---|---|---|---|---|
| $E_{relative}$ (crystal) | 0.00 | 40.77 | →**AlCu(II)-1** | 46.61 | 46.39 |
| $E_{relative}$ (cluster) | 0.00 | 51.84 | →**AlCu(II)-1** | 55.58 | 77.35 |

**Fig. 5.** Possible Cu(II) binding locations (with 2-Al support) and relative energies estimated in kcal mol$^{-1}$.

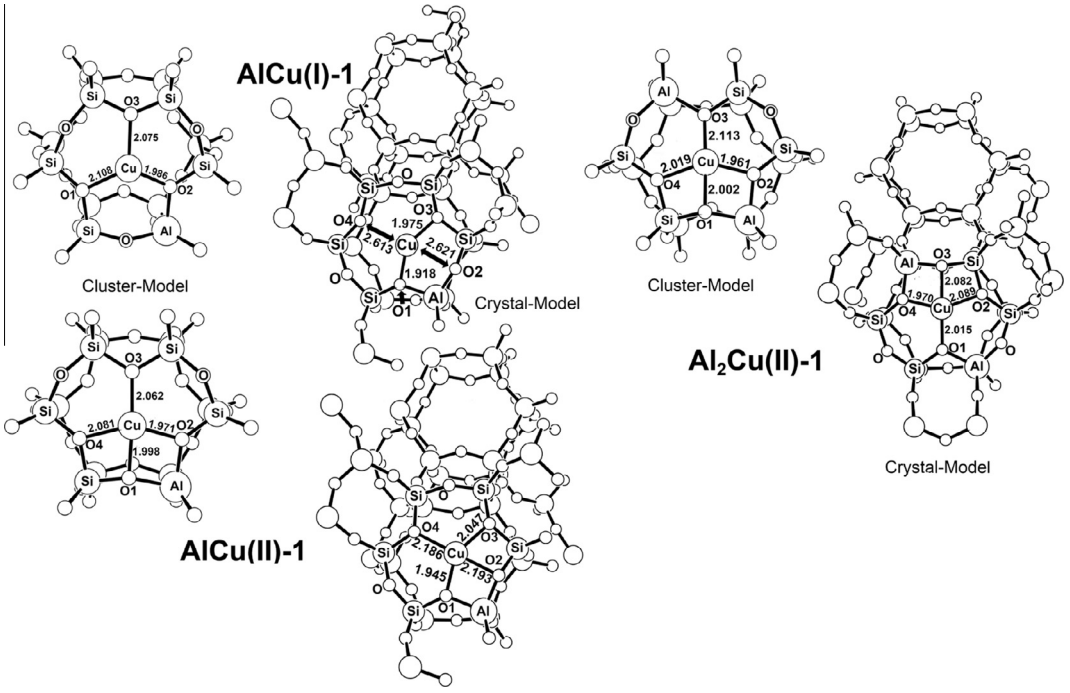


**Fig. 6.** Optimized structures of cluster and crystal models of **AlCu(I)-1**, **AlCu(II)-1**, **$Al_2Cu(II)$-1**.

copper center in **X1** must be of higher oxidation state than Cu(I), suggesting possibly a Cu(II)–NO motif. Among the IR-modes associated with species that exist after the NO-reduction reaction is complete, there is a peak at 1905/1890 cm$^{-1}$ that grows in within the first 10 min and remains visible consistently throughout the experiment. This spectroscopic feature appears to be associated with a different species than **X1**, but may also contain a Cu(II)–NO fragment, judging from the frequency. Thus, this final

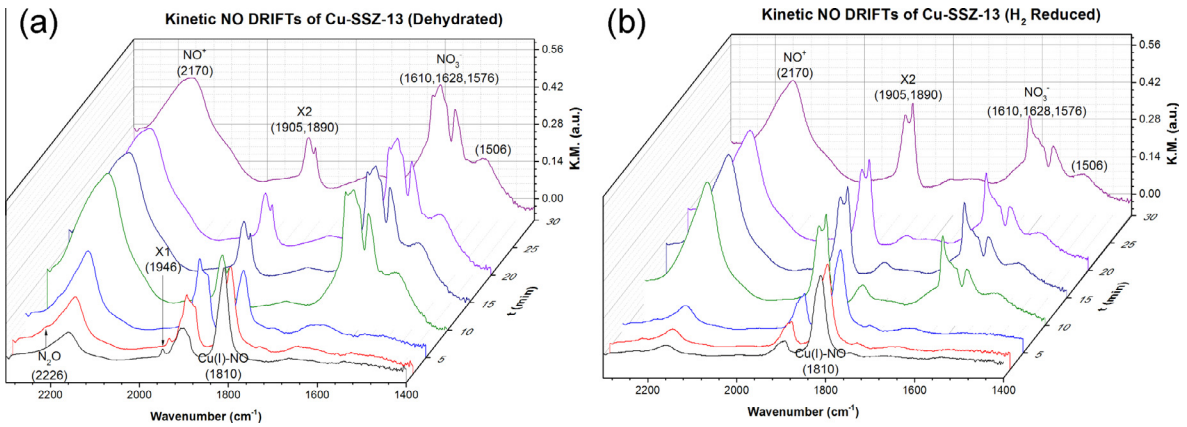


**Fig. 7.** Kinetic DRIFTs of NO reduction with Cu-SSZ-13 (a: dehydrated; b: $H_2$ reduced).

NO-bound species that we labeled **X2** must be structurally different from the fleeting intermediate associated with the 1946 $cm^{-1}$ mode – it is not clear what this difference may be (*vide infra*). The broad features in the region of 1500–1600 $cm^{-1}$ that appear after 10 min of NO exposure are assigned to be adsorbed surface nitrates ($NO_3^-$), identifying $NO_3^-$ as an immediate product at $t$ = 5 min. Perhaps the most dominating feature in this series of time resolved IR-spectra is the appearance of a broad and intense stretching band at ~2170 $cm^{-1}$, which grows into the spectrum and appears to reach saturation levels after $t$ = 10 min. At such a high frequency, there are not many M–NO species imaginable (*vide infra*) – the $NO^+$ cation displays a N–O stretching frequency of ~2300 $cm^{-1}$ and we consequently assign this broad feature to a weakly adsorbed $NO^+$ species within the zeolite framework. $H_2$ reduced Cu-SSZ-13 shows a similar dynamic pattern in the kinetic DRIFTs experiment ( Fig. 7b), except that the amount of the transient **X1** species at 1946 $cm^{-1}$ is significantly reduced, further inferring that Cu in a high oxidation state, e.g. Cu(II), is involved.

Based on the above described synchronized dynamic behavior of different Cu species, it is reasonable to assume that Cu(I) formed by self-reduction of Cu(II) at the preferred zeolite location binds NO and undergoes a series of chemical reactions to generate higher oxidation state copper centers, possibly Cu(II). The final products of this trapped portion of the catalytic cycle are $NO^+$ and nitrate. Whereas this insight is helpful, as it directly identifies the species present during the NO reduction process, it is impossible to attribute the observed vibrational frequencies to the identity and structure of an intermediate in a precise manner. Thus, we carried out quantum chemical studies to augment these spectroscopic results with the following aims: (1) derive a precise structural representation of each assigned intermediate seen in the DRIFTs experiment, (2) identify where the redox chemistry occurs on the Cu center, i.e. examine the electronic structure of each intermediate to assign the oxidation states of the copper site, (3) identify the role of NO during the sequence of reaction; (4) characterize the final $NO^+$ product, which will be highly reactive towards $NH_3$ and continue the catalytic cycle if $NH_3$ were present. These questions are extremely challenging, if not impossible to answer precisely with currently available experimental methods. We can use the observed vibrational frequencies as benchmarks for our quantum chemical calculations, however, to produce such detailed information. We can explore numerous Cu–NO binding motifs and calculate the vibrational frequencies to relate our computations to the DRIFTs data. Previously, Peden and co-workers suggested that Cu may bind within an 8-membered ring of the zeolite framework and compared vibrational frequencies from IR spectroscopy with DFT calculations. They achieved good matches with several of the observed intermediates, but their computational models did not give any results that resembled the experimentally observed $NO^+$ stretching frequency at ~2170 $cm^{-1}$ [60].

Currently available computational methods, such as Density Functional Theory (DFT), are quite robust and are widely used to compute molecular structures and reaction energies. NO is an interesting substrate as it can adopt three fundamentally different modes of binding when interacting with a Cu(II) atom: (i) The simplest binding mode is realized when the NO acts as a "normal" Lewis-base ligand using one of its doubly-occupied lone pair orbitals on nitrogen and forms a dative bond with the Lewis-acidic metal center, where no redox reaction takes place. The formal oxidation state of the metal center does not change, thus affording a Cu(II)–NO fragment where the radical character across the [NO] fragment is maintained. (ii) A second possible and common binding mode involves the transfer of an electron from the metal center to the NO-fragment to formally afford a $[NO]^-$ ligand that is bound to a metal center, thus yielding a Cu(III)–$[NO]^-$ fragment that has no radical character whatsoever. This binding mode results in a bent coordination geometry, where the M–N–O angle deviates significantly from 180°. (iii) Lastly, NO may bind reductively by transferring an electron to the metal site to e.g. form Cu(I)–$[NO]^+$, where the oxidation state of the metal is decreased and the M–N–O angle becomes 180°. Whereas quantum chemical methods are capable of reproducing all three binding modes reliably, allowing for predicting and understanding which binding mode will be preferred [61], there is currently no intuitive way of predicting which binding mode will be adopted without carrying out the calculation explicitly. Clearly, the redox-potential of the copper center that is in turn governed by the specific ligand environment at any given structure will play a pivotal role in determining whether the NO-ligand bound to it is formally neutral, cationic or anionic, but there are other factors, such as the coordination geometry of the copper center and/or which alternative ligands are available, that will play an equally important role. As the oxidation state of the NO molecule has a decisive impact on its reactivity e.g. towards ammonia and other equivalents of NO, it is important that we understand which electronic structure is adopted in each of the intermediates and our computer models are well-prepared to provide answers to this complex question, as will be highlighted below.

Calculating harmonic vibrational frequencies from quantum chemical models can be considered routine [62,63]. However, studies where the vibrational frequencies derived from IR-spectra and computations are compared systematically to identify the surface-bound intermediates of a complex reaction are rare [64–68]. Thus, to first identify which computational methodology should be used, we have carried out several benchmark calculations – within the DFT framework, the most important decision to be made relates to the exchange–correlation functional, which has a

profound influence on the reliability of the computed results [69–71]. Among the many that we have sampled, results using two popular functionals, namely B3LYP [72–75] and PBE [45], are compared in Table 1. Both functionals produce reasonable results with the RMSD of the computed versus experimental frequencies being 41 and 27 $cm^{-1}$, respectively. PBE gives a slightly better match with the experimental frequencies: For example, free NO· is calculated to have a N–O stretching frequency of 1882 $cm^{-1}$ with PBE, in excellent agreement with the experimental value of 1876 $cm^{-1}$ [40], whereas 1920 $cm^{-1}$ is obtained with B3LYP. A similar trend is observed for various small molecule systems enumerated in Table 1, suggesting that the PBE results are most convenient for our work. Note that while better correlation with experimental values seen for the PBE functional is undeniable, the differences between the two functionals are small considering that the RMSD difference of 14 $cm^{-1}$ only corresponds to energy differences of 0.04 kcal $mol^{-1}$. Thus, this slightly different performance should not be over-interpreted. To compare the performance of our computer models when the transition metals are included, we considered an additional model compound: The structurally well-characterized mononuclear copper nitrosyl complexes [76] shown in Fig. 8 display distinctive NO frequencies, which are again well reproduced by the PBE functional with a deviation of no more than 31 $cm^{-1}$, whereas B3LYP shows a slightly larger discrepancy.

In this work, we focus on the early portion of the SCR process, which involves the consumption of six molecules of NO. In the catalytic reaction, the chemical driving force is provided by two equivalents of ammonia to produce three molecules of $N_2O$ and $H_2O$, in addition to one $N_2$, as summarized in Scheme 1. In the DRIFTs experiment described above, the lack of ammonia interrupts the catalytic conversion and various reactive intermediates are trapped in a stoichiometric fashion. Before the Cu-assisted SCR reactions are explored, it is helpful to consider the uncatalyzed energy and oxidation state changes that must occur. We assume that sequential, multiple NO adsorptions can occur on the active Cu site of Cu-CHA, which is a reasonable assumption given the abundant NO flow in the DRIFTs experiment. A similar sequence of multiple NO binding was previously observed on related Cu-ZSM-5 systems [77–79]. A plausible scheme leading to the intermediates formed at this early stage of the reaction is shown in Scheme 1. Forming nitrous oxide ($N_2O$) from two molecules of NO is formally a two-electron reduction, as two N(+II) atoms are formally converted to a (−I)N = N(+III) moiety, that is one N undergoes a one-electron oxidation, whereas the other is reduced formally by 3 electrons ( Scheme 1a, in blue). To accomplish this reaction in a stoichiometrically balanced fashion, one excess oxygen atom must be released – in the catalytic process, this task is likely accomplished by ammonia, but in absence thereof, another equivalent of NO can serve as the oxygen-acceptor to form the nitrite anion, where one electron must be supplied for example by a Cu(I)-center, as shown in Scheme 1b. The nitrite anion can be used to accept a second oxygen atom, forming the nitrate anion and allowing two more NO equivalents to be reduced to nitrous oxide. To maintain mass and electron balance for the reactions outlined in Scheme 1a and b, we must recruit an electron from oxidizing one equivalent of NO, producing $NO^+$ in the process, as outlined in Scheme 1c. These three putative transformations provide a conceptual framework for the Cu-mediated reactions that will be discussed below. An energetically viable transformation of these intermediate products with ammonia is shown in Scheme 1d. The overall energy of these processes are calculated to be −204.1 kcal $mol^{-1}$ – oxidation of two equivalents of ammonia provides more than enough energy to drive this reaction. These energies are computed using CCSD(T)/cc-pVQZ level of theory, which is more accurate, but also much more expensive computationally. A systematic comparison shows that the errors produced by the cheaper DFT-methods that we use for the large simulations are acceptable (see Supporting Information for details).

Our extensive computational explorations aimed at identifying energetically viable pathways to obtaining the intermediates identified above suggest that the overall reaction should be divided into two half-reactions: In the first half reaction, summarized in Scheme 2, the zeolite-supported Cu(I) species **1** binds three NO molecules to ultimately afford compound **4**. By carefully analyzing the electronic structure of the lowest energy geometry that we obtained from our calculations at each stage of the reaction pathway, we can assign formal oxidation states to both the NO and copper fragments, which in turn allows for understanding the energetics of each step in an intuitively comprehensible fashion: The free energy of binding the first equivalent of NO to compound **1** is downhill by −10.7 kcal $mol^{-1}$. A Mulliken spin density of 0.914 on the NO fragment in **2** indicates that this binding event is not associated with a redox event and that the Cu(I) center simply acts as a Lewis acid. We were able to locate an isomeric structure **2a**, where the copper center moves closer to the Al-substituted site, which was 8.2 kcal $mol^{-1}$ higher in energy than **2**. This structural arrangement is the first of many illustrating the relatively high mobility of the Cu-ion within the zeolite framework. To push the reaction forward, compound **2** must bind a second equivalent of NO to give **3**. This step is only viable if the oxidation state of the copper center changes to Cu(III), that is unlike the first NO-binding, this step represents an oxidative addition where one electron is moved from the Cu(I) center to the incoming NO and another is moved to the NO ligand that is already bound to copper, to form a Cu(III)–$[NO^-]_2$ fragment. The Cu–N–O bond angle is reduced from

**Table 1**
Computed vibrational frequencies vs. experimental values in $cm^{-1}$.

| | Exp. | B3LYP | | PBE | |
|---|---|---|---|---|---|
| | | Calculated | Δ | Calculated | Δ |
| NO | 1876 [40] | 1920 | 44 | 1882 | 6 |
| $NO^+$ | 2345 [40] | 2386 | 41 | 2330 | −15 |
| $NO^-$ | 1363 [40] | 1408 | 45 | 1388 | 25 |
| $NO_3^-$ | 1356 [41] | 1417 | 61 | 1398 | 42 |
| $NO_2^-$ | 1284 [42] | 1322 | 38 | 1288 | 4 |
| 1242 [41] | 1288 | 46 | 1228 | −14 | |
| 776 [42] | 756 | −20 | 743 | −33 | |
| $N_2O$ | 2224 [43] | 2280 | 56 | 2277 | 53 |
| 1285 [43] | 1292 | 7 | 1301 | 16 | |
| 589 [43] | 577 | −12 | 578 | −11 | |
| RMSD | | | 41 | | 27 |

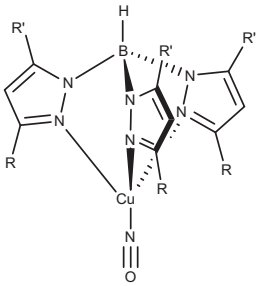


$Tp^{t\text{-}Bu}$ (R = *t*-Bu, R' = H)
$Tp^{Ph2}$ (R = R' = Ph)

| Structure | Experiment | B3LYP | PBE |
|---|---|---|---|
| $Tp^{t\text{-}Bu}$ | 1712 | 1798 | 1743 |
| $Tp^{Ph2}$ | 1720 | 1807 | 1744 |

**Fig. 8.** Experimental [76] vs. computed vibrational frequencies of Cu nitrosyl in $cm^{-1}$.

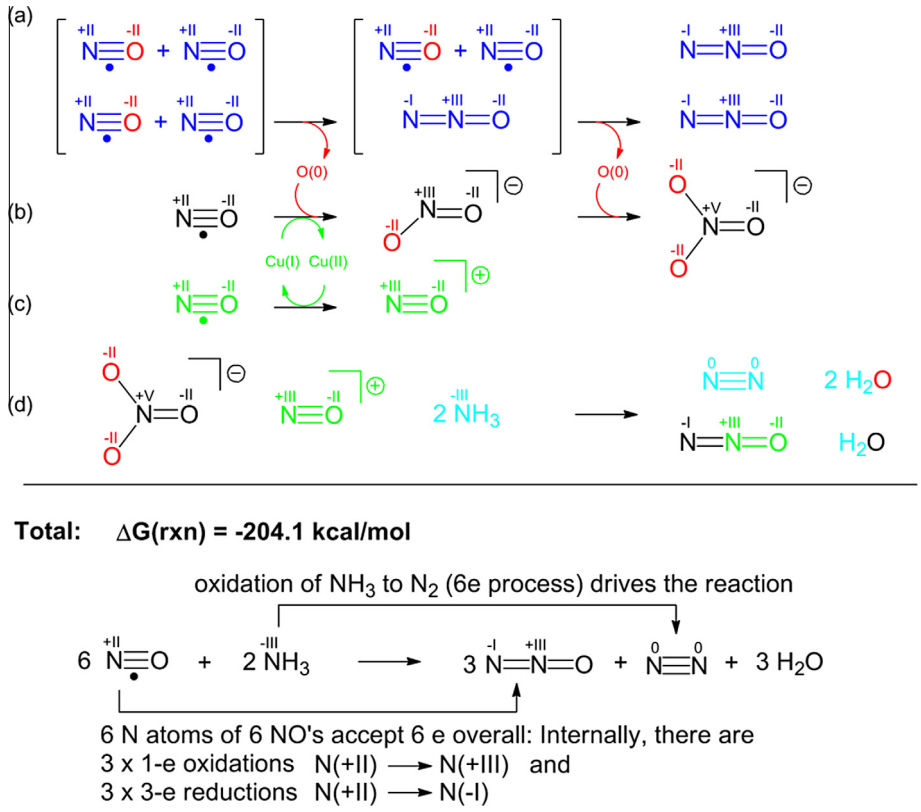


**Scheme 1.** Thermodynamics of the overall reaction.

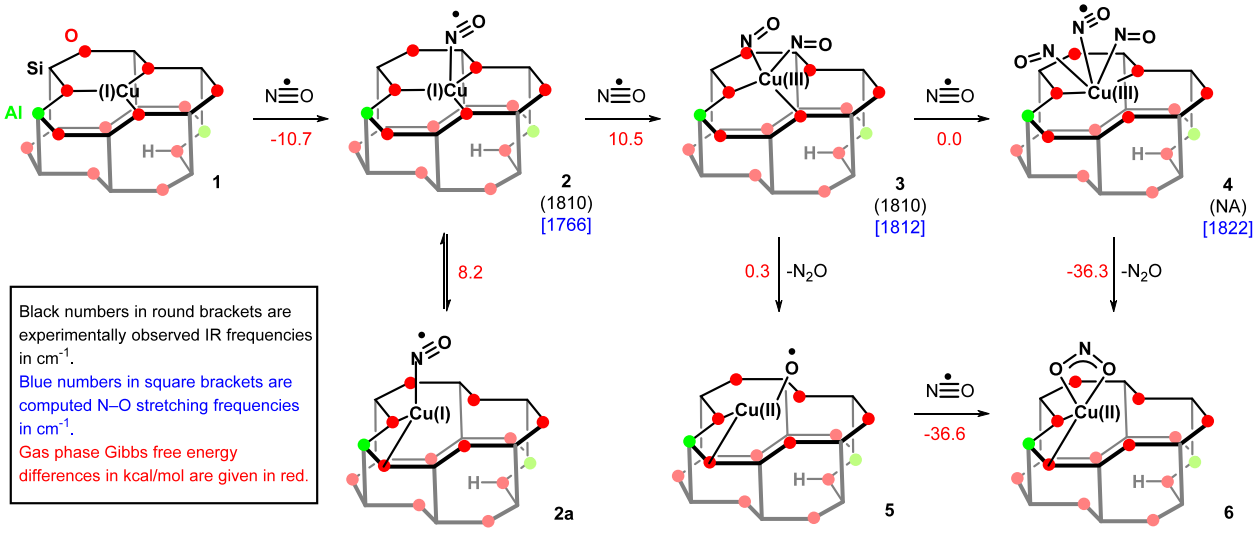


**Scheme 2.** A proposed reaction scheme for first half reaction in DRIFTs experiment with estimated free energy change by PBE.

131° in **2** to an average of 121° in **3**, consistent with reduction of the nitrosyl ligands. Additionally, the electrostatic atomic charge on Cu increases from 0.449 to 0.503. We propose that accessing this Cu(III) manifold is important, as it transforms the Cu(I)-$d^{10}$ center that is incapable of binding more than one NO-ligand to a Cu(III)-$d^8$ center, which can bring together multiple NO equivalents at a single center. Our calculations indicate that the step **2** → **3** is thermodynamically uphill by 10.5 kcal $mol^{-1}$. As the electronic structure distortion is significant for this process, we expect that the barrier for this step will be significant, although we do not expect it to be rate determining. Consequently, species **2** should exhibit a finite life time and accumulate as a detectable intermediate in equilibrium with species **3**. The N–O stretching frequencies of these two intermediates were computed to be 1766 and 1812 $cm^{-1}$, respectively, which we assign to the IR-band detected at 1810 $cm^{-1}$ upon exposing Cu-SSZ-13 to NO. Note that we had tentatively assigned the 1810 $cm^{-1}$ mode to a Cu(I)–NO species, simply based on the notion that a weakly bound NO should display a vibrational mode in this region of the IR-spectrum.

Our calculations show that this expectation is well-founded and furthermore suggest that the initial NO-binding may be more complicated than anticipated in that species **3**, which contains two

formally anionic [$NO^-$] ligands bound to a Cu(III) center and displays N–O stretching frequencies that are very close to that of **2**, exists in equilibrium. Cu(III) dinitrosyls have previously been observed with FTIR in Cu-ZSM-5 [80].

Compound **3** can bind an additional NO molecule to give compound **4** or eliminate $N_2O$ to from a Cu(II)-Oxyl complex **5** in an energetically neutral process – either way leads immediately to the formation of intermediate **6**, the Cu(II)-nitrito complex, which is thermodynamically downhill by nearly 37 kcal $mol^{-1}$. Thus, we do not expect compounds **4** or **5** to be detectable. During the step **4** → **6**, which is formally a reductive elimination, two of the NO ligands are transformed into a single molecule of $N_2O$ and the third NO moiety bound to Cu(III) in **4** serves as the oxygen-acceptor, forming a nitrite ($NO_2^-$) group. The oxidation state of N changes from N(+II) to N(+III), thus providing one of the required two electrons for the generation of $N_2O$. The second electron comes from the copper center – in a classical reductive elimination process, the Cu(III) center becomes Cu(I), but because the copper center provides the second electron for the reductive generation of $N_2O$, the copper center in **5** is formally in an oxidation state of (+II). This first step of the catalysis can therefore be summarized as:

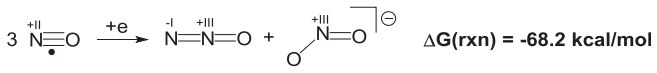


Thermodynamically, this gas-phase reaction is downhill by 68.2 kcal $mol^{-1}$ (CCSD(T)/cc-pVQZ). To relate this energy to our proposed catalytic cycle, we have to consider that the nitrite anion is bound to the Cu(II) center and the copper center has been oxidized. Our calculations indicate that the reaction free energy of **1** → **6** is −36.3 kcal $mol^{-1}$, which is reasonable, given the thermodynamics of the substrate transformations. Note, that this mechanism assigns different roles to the three NO molecules: Two become substrates that are converted to $N_2O$, whereas one NO serves as the oxygen-acceptor.

As shown in Scheme 3, the catalytic cycle proceeds by compound **6** accepting two more NO molecules to form intermediate **8**, where one $(NO)^-$, one $(NO)^{\cdot}$ and one nitrito ligands are bound to a Cu(III)-center. Intermediate **7** should be detectable, as the next steps involve reactions that we expect to be associated with significant reaction barriers. The most characteristic N–O stretching frequency of the [$NO_2$]Cu–NO moiety is calculated to be 1915 $cm^{-1}$ and we propose that this species is what was labeled as **X1** with an experimental IR-stretching mode at 1946 $cm^{-1}$, which accumulates as a fleeting intermediate within the first 10 min of adding NO to zeolite supported Cu. As we had speculated, the copper in this intermediate is in a higher oxidation state, but our calculations are most consistent with a Cu(III)-center rather than a Cu(II)-center. Intermediate **7** can readily form the second equivalent of the $N_2O$ product according to:

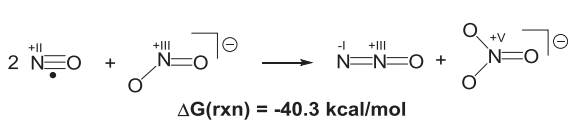


The nitrito ligand again serves as the oxygen-acceptor and accommodates the superfluous oxygen atom to become a nitrato ligand. Unlike in the first cycle of the reaction, the nitrogen atom of the nitrite is also the reducing agent and provides the two electrons needed to form $N_2O$ from 2 NO molecules. This process may be accomplished by intermediate **7** binding another NO molecule to give the Cu(III)-nitrito intermediate **8**, which should immediately liberate one equivalent of $N_2O$ and form the Cu(II)-nitrato complex **9** with a reaction free energy of −39.3 kcal $mol^{-1}$. Binding of the last equivalent of NO (intermediate **10**) followed by elimination of nitric acid using a zeolite bound proton gives species **11**, which has a N–O stretching mode at 1920 $cm^{-1}$ and we assign this species to be compound **X2** associated with the IR-spectroscopic feature seen at the 1905/1890 $cm^{-1}$ in the later phase of the DRIFTs experiment. Finally, the Cu(III)–NO fragment in **11** can rearrange at a moderate thermodynamic cost of 3.3 kcal $mol^{-1}$ to afford the final product **12**, where the Cu(III) center was reduced to Cu(I) and $NO^+$ is formed by placing the Cu(I) and $NO^+$ cations on each of the two six-membered rings of the aluminum-doped chabazite framework. By accessing a Cu(III) center it is possible to reductively eliminate the NO ligand to regenerate Cu(I) without involving a copper dimer [81]. The complete thermodynamic profile for all of the transformations using the cluster model described in Schemes 2 and 3 is shown in Fig. 9 along with the optimized structure of the proposed $NO^+$ intermediate **12**.

The N–O vibrational frequency of species **12** is calculated to be 2159 $cm^{-1}$ and we suggest that intermediate **12** is the final product complex that gives rise to the dominating IR-spectral feature at 2170 $cm^{-1}$. The computed geometry is shown in Fig. 9. This is the first time that a detailed structure of the intermediate with the observed IR stretching frequency at 2170 $cm^{-1}$ is proposed. A weak electrostatic interaction between $NO^+$ and the Al-doped, and thus, negatively polarized zeolite framework, holds the $NO^+$ in place with the most positive end of the molecular cation facing the Al-substituted edge of the six-membered ring structure. The N–O bond length of 1.106 Å is very close to the bond length of 1.085 Å expected for free $NO^+$ in gas phase. The distance between the NO-nitrogen and the nearest oxo of the zeolite is 2.050 Å, which is basically at the van der Waals contact distance. The distance between the NO-oxygen and the nearest oxo within the six-membered zeolite ring is 2.573 and 2.829 Å, as illustrated in Fig. 9. This proposal is different from previously imagined structures for the $NO^+$ trapping intermediates. One proposal was that $NO^+$ may be trapped within a larger zeolite cage [27] – our calculations indicate that the electrostatic forces in the undoped chabazite are too delocalized and consequently too weak to hold $NO^+$ in a well-defined position without the additional negative charge that is introduced by Al-doping. The additional aluminate site also may help overcome the need to invoke copper oxide clusters in order to oxidize NO. Despite significant efforts, we were unable to locate a proper minimum that produced a vibrational frequency matching the one experimentally observed. Another popular proposal is that $NO^+$ may be compounded with either $NO_2$ or $N_2O_4$ in the gas phase [82], which we have considered specifically in our calculations. Fig. 10a shows the optimized structure of such putative [$NO^+$]–[$NO_2^-$] adduct and its computed vibrational frequencies. The interactions between the two molecular units are quite strong, resulting in an elongated N–O bond of 1.149 Å. The vibrational frequency computed to be 1895 $cm^{-1}$. Another plausible adduct, [$NO^+$]–[$N_2O$], was also considered, as shown in Fig. 10b, and found to be not a likely candidate to explain the experimentally observed IR-band at 2170 $cm^{-1}$.

Intermediate **12** is mechanistically important, as it will likely be the primary reactant that will carry the catalytic reaction forward if ammonia is present, especially at the desirable low temperature conditions. In our attempt to identify the $NO^+$-trapping structure that displays a vibrational frequency in the 2170 $cm^{-1}$ range, we considered many plausible species and found that the $NO^+$-vibration is extremely sensitive to environmental influence. Any pointed electrostatic interaction between a negatively polarized entity and the $NO^+$ cation led to vibrational frequencies in the 1900 $cm^{-1}$ range or even lower, as highlighted above in the case of the

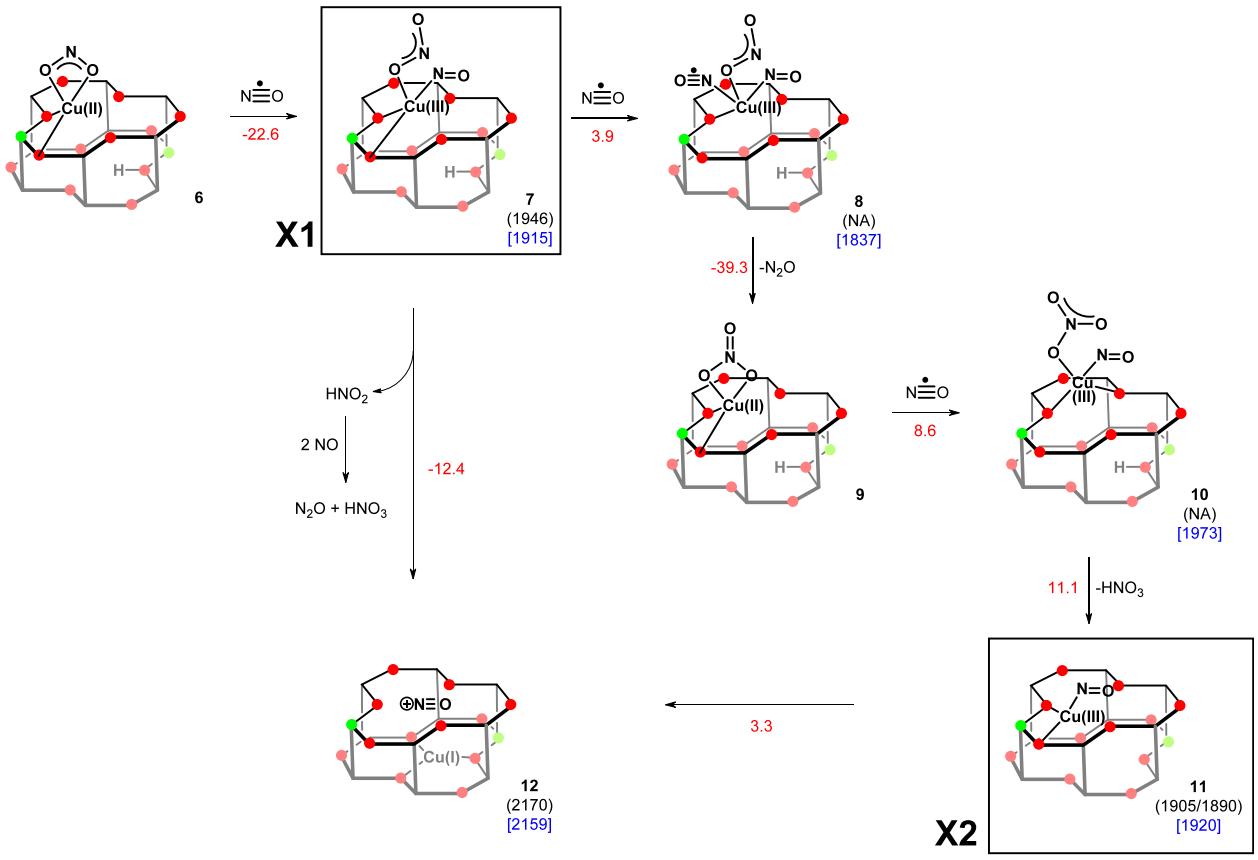


**Scheme 3.** A proposed reaction scheme for second half reaction in DRIFTs experiment with estimated free energy change by PBE.

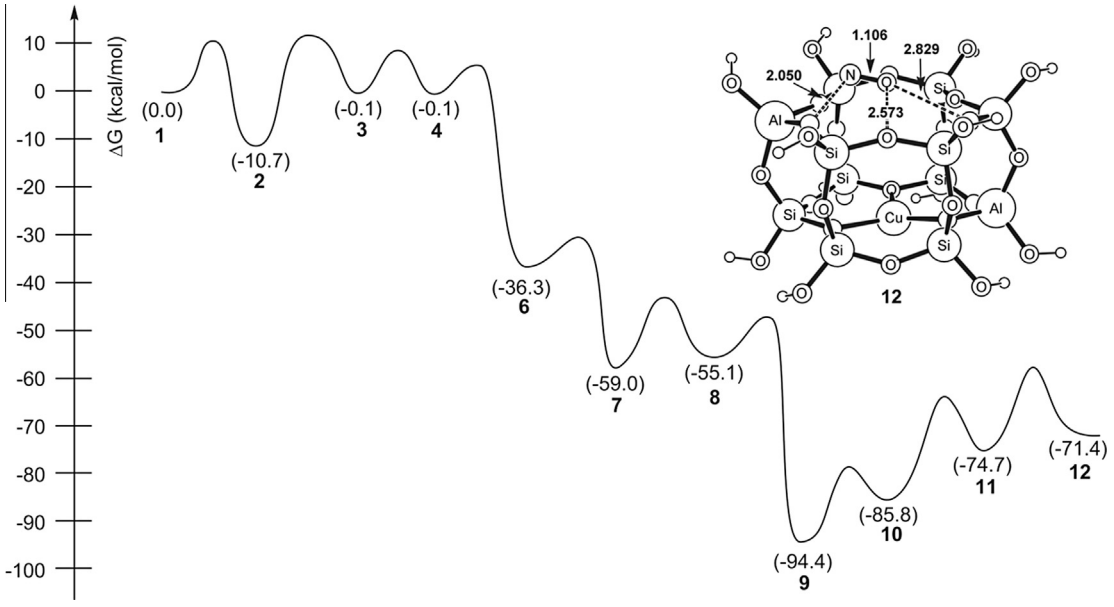


**Fig. 9.** Energy profile for proposed catalytic cycle in kcal $mol^{-1}$. Bond lengths for optimized structure of proposed intermediate **12** are given in Å.

$[NO^+]$–$[NO_2^-]$ adduct. In **12**, the Al-doped chabazite cell provides just enough negative charge to hold the $NO^+$ cation in place, while the delocalization of that charge into the six-membered ring makes it impossible for $NO^+$ to recruit electron density and lose the cationic character. We speculate that this is a key characteristic of the d6R unit in Cu-SSZ-13 catalyst, as preserving the cationic character of the $NO^+$ and holding it at a steady, well-defined position will be critically important for allowing a smooth, low-barrier reaction with the nucleophilic $NH_3$ substrate. In the current study, we have not attempted to address this second phase of the catalytic reaction and we have not identified any transition states – these more advanced studies, that will ultimately allow for deriving answers

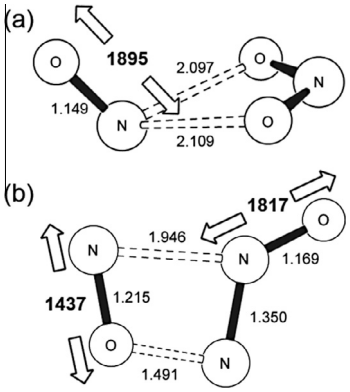


**Fig. 10.** Computed structure (bond lengths in Å) and vibrational frequencies (in $cm^{-1}$) of a putative $[NO^+]$–$[N_2O]$ adduct.

to the challenge questions mentioned in the introduction, are now possible with plausible intermediate structures being identified.

## 4. Conclusion

Quantum chemical models characterizing the active site Cu-doped Cu-SSZ-13 catalyst were developed and benchmarked to match vibrational spectra from DRIFTs measurements. This approach enables the plausible assignment of tentative intermediates to experimentally observed vibrational modes with information as to which steps in the catalytic cycle the redox chemistry occurs at the metal center. Key among these identified intermediates is a $NO^+$ trapped intermediate that is supported by the negative charge delocalized through the Al-doped chabazite. This oxidized NO fragment with a computationally characterized stretching frequency of 2159 $cm^{-1}$ (exp. 2170 $cm^{-1}$) is likely to be essential for the rapid reaction of $NH_3$ en route to $N_2$ formation. Further studies will assess the mechanism of formation for this and other identified intermediates with the idea of using such understanding to rationally optimize the Cu-SSZ-13 catalyst for enhanced SCR performance.

## Acknowledgments

We thank the NSF(0116050, CHE-0645381, CHE-1001589), the Research Corporation (Scialog Award to MHB), the National Research Foundation of Korea for a WCU Award to Korea University (R31-2012-000-10035-0) and the BASF Corporation for support.

## Appendix A. Supplementary data

Supplementary data associated with this article can be found, in the online version, at http://dx.doi.org/10.1016/j.ica.2015.02.021.

## References

[1] P. Granger, V.I. Parvulescu, Chem. Rev. 111 (2011) 3155.
[2] R. Burch, Catal. Rev. – Sci. Eng. 46 (2004) 271.
[3] S. Brandenberger, O. Krocher, A. Tissler, R. Althoff, Catal. Rev. – Sci. Eng. 50 (2008) 492.
[4] S. Roy, A. Baiker, Chem. Rev. 109 (2009) 4054.
[5] E. Tronconi, I. Nova, C. Ciardelli, D. Chatterjee, B. Bandl-Konrad, T. Burkhardt, Catal. Today 105 (2005) 529.
[6] D.A. Peña, B.S. Uphade, P.G. Smirniotis, J. Catal. 221 (2004) 421.
[7] G. Busca, L. Lietti, G. Ramis, F. Berti, Appl. Catal. B 18 (1998) 1.
[8] L. Casagrande, L. Lietti, I. Nova, P. Forzatti, A. Baiker, Appl. Catal. B 22 (1999) 63.
[9] C. Ciardelli, I. Nova, E. Tronconi, D. Chatterjee, B. Bandl-Konrad, M. Weibel, B. Krutzsch, Appl. Catal. B 70 (2007) 80.
[10] M. Iwamoto, H. Furukawa, Y. Mine, F. Uemura, S. Mikuriya, S. Kagawa, J. Chem. Soc., Chem. Commun. 16 (1986) 1272.
[11] M. Iwamoto, H. Yahiro, Y. Mine, S. Kagawa, Chem. Lett. 18 (1989) 213.
[12] M. Iwamoto, H. Yahiro, K. Tanda, N. Mizuno, Y. Mine, S. Kagawa, J. Phys. Chem. 95 (1991) 3727.
[13] X. Yang, Z. Wu, M. Moses-Debusk, D.R. Mullins, S.M. Mahurin, R.A. Geiger, M. Kidder, C.K. Narula, J. Phys. Chem. C 116 (2012) 23322.
[14] J.M. García-Cortés, J. Pérez-Ramírez, M.J. Illán-Gómez, F. Kapteijn, J.A. Moulijn, C. Salinas Martínez de Lecea, React. Kinet. Catal. Lett. 70 (2000) 199.
[15] I. Bull, W.-M. Xue, P. Burk, R.S. Boorse, W.M. Jaglowski, G.S. Koermer, A. Moini, J.A. Patchett, J.C. Dettling, M.T. Caudle, 2009; Vol. Us7601662b2.
[16] U. Deka, A. Juhin, E.A. Eilertsen, H. Emerich, M.A. Green, S.T. Korhonen, B.M. Weckhuysen, A.M. Beale, J. Phys. Chem. C 116 (2012) 4809.
[17] S.T. Korhonen, D.W. Fickel, R.F. Lobo, B.M. Weckhuysen, A.M. Beale, Chem. Comm. 47 (2011) 800.
[18] J. Hun Kwak, H. Zhu, J.H. Lee, C.H.F. Peden, J. Szanyi, Chem. Comm. 48 (2012) 4758.
[19] F. Giordanino, P.N.R. Vennestrom, L.F. Lundegaard, F.N. Stappen, S. Mossin, P. Beato, S. Bordiga, C. Lamberti, Dalton Trans. 42 (2013) 12741.
[20] V.F. Kispersky, A.J. Kropf, F.H. Ribeiro, J.T. Miller, Phys. Chem. Chem. Phys. 14 (2012) 2229.
[21] D.W. Fickel, E. D'addio, J.A. Lauterbach, R.F. Lobo, Appl. Catal. B 102 (2011) 441.
[22] Q. Ye, L. Wang, R.T. Yang, Appl. Catal. A 427–428 (2012) 24.
[23] F. Gao, E.D. Walter, N.M. Washton, J. Szanyi, C.H.F. Peden, Acs Catalysis 3 (2013) 2083.
[24] J.H. Kwak, R.G. Tonkyn, D.H. Kim, J. Szanyi, C.H.F. Peden, J. Catal. 275 (2010) 187.
[25] J. Kwak, D. Tran, J. Szanyi, C.F. Peden, J. Lee, Catal. Lett. 142 (2012) 295.
[26] J.S. Mcewen, T. Anggara, W.F. Schneider, V.F. Kispersky, J.T. Miller, W.N. Delgass, F.H. Ribeiro, Catal. Today 184 (2012) 129.
[27] J.H. Kwak, J.H. Lee, S.D. Burton, A.S. Lipton, C.H.F. Peden, J. Szanyi, Angew. Chem., Int. Ed. 52 (2013) 9985.
[28] F. Göltl, R.E. Bulo, J. Hafner, P. Sautet, J. Phys. Chem. Lett. 4 (2013) 2244.
[29] F. Göltl, J. Hafner, J. Chem. Phys. 136 (2012) 064501.
[30] F. Göltl, J. Hafner, J. Chem. Phys. 136 (2012) 064502.
[31] F. Göltl, J. Hafner, J. Chem. Phys. 136 (2012) 064503.
[32] D.W. Fickel, R.F. Lobo, J. Phys. Chem. C 114 (2009) 1633.
[33] R.M. Kakwani, K.C. Voss, J.A. Patchett, K.R. Grimston, 2004; Vol. Us6826906b2.
[34] J.H. Kwak, D. Tran, J. Szanyi, C.H.F. Peden, J.H. Lee, Catal. Lett. 142 (2012) 295.
[35] P. Broqvist, H. Gronbeck, E. Fridell, I. Panas, Catal. Today 96 (2004) 71.
[36] K. Tian, X.-Y. Tu, S.-S. Dai, Surf. Sci. 601 (2007) 3186.
[37] C. Popa, A.P. Van Bavel, R.A. Van Santen, C.F.J. Flipse, A.P.J. Jansen, Surf. Sci. 602 (2008) 2189.
[38] A. Eichler, J. Hafner, Chem. Phys. Lett. 343 (2001) 383.
[39] R.G. Parr, W. Yang, Density Functional Theory of Atoms and Molecules, Oxford University Press, New York, 1989.
[40] T. Ziegler, Chem. Rev. 91 (1991) 651.
[41] B.M. Mark, In Structure-Property Relations In Polymers; American Chemical Society: 1993; vol. 236, p. 351.
[42] M.P. Fuller, P.R. Griffiths, Anal. Chem. 1978 (1906) 50.
[43] M. Schmal, M.A.S. Baldanza, M.A. Vannice, J. Catal. 185 (1999) 138.
[44] Schrödinger Inc., Portland, Oregon, 2013.
[45] J.P. Perdew, K. Burke, M. Ernzerhof, Phys. Rev. Lett. 77 (1996) 3865.
[46] W.J. Hehre, R. Ditchfield, J.A. Pople, J. Chem. Phys. 56 (1972) 2257.
[47] P.J. Hay, W.R. Wadt, J. Chem. Phys. 82 (1985) 270.
[48] P.J. Hay, W.R. Wadt, J. Chem. Phys. 82 (1985) 299.
[49] T.H. Dunning Jr., J. Chem. Phys. 90 (1989) 1007.
[50] Nist Computational Chemistry Comparison and Benchmark Database Nist Standard Reference Database Number 101 Release 16a, A., Editor: Russell D. Johnson Iii. http://Cccbdb.Nist.Gov/.
[51] G. Kresse, J. Hafner, Phys. Rev. B 48 (1993) 13115.
[52] G. Kresse, J. Furthmüller, Comput. Mater. Sci. 6 (1996) 15.
[53] P.E. Blöchl, Phys. Rev. B 50 (1994) 17953.
[54] G. Kresse, D. Joubert, Phys. Rev. B 59 (1999) 1758.
[55] K. Raghavachari, G.W. Trucks, J.A. Pople, M. Head-Gordon, Chem. Phys. Lett. 157 (1989) 479.
[56] F. Neese, A. Hansen, F. Wennmohs, S. Grimme, Acc. Chem. Res. 42 (2009) 641.
[57] B.R. Goodman, K.C. Hass, W.F. Schneider, J.B. Adams, Catal. Lett. 68 (2000) 85.
[58] D.W. Fickel, J.M. Fedeyko, R.F. Lobo, J. Phys. Chem. C 114 (2010) 1633.
[59] R. Zhang, J.-S. Mcewen, M. Kollár, F. Gao, Y. Wang, J. Szanyi, C.H.F. Peden, Acs Catalysis (2014) 4093.
[60] R. Zhang, J.-S. Mcewen, M. Kollár, F. Gao, Y. Wang, J. Szanyi, C.H.F. Peden, Acs Catalysis 4 (2014) 4093.
[61] M.H. Lim, B.A. Wong, W.H. Pitcock Jr., D. Mokshagundam, M.-H. Baik, S.J. Lippard, J. Am. Chem. Soc. 128 (2006) 14364.
[62] A.P. Scott, L. Radom, J. Phys. Chem. 100 (1996) 16502.
[63] J. Neugebauer, B.A. Hess, J. Chem. Phys. 118 (2003) 7215.
[64] J.M. Perez, K. Somasundram, V. Termath, N.C. Handy, D.A. King, Surf. Sci. 380 (1997) 83.
[65] P. Pietrzyk, C. Dujardin, K. Gora-Marek, P. Granger, Z. Sojka, Phys. Chem. Chem. Phys. 14 (2012) 2203.
[66] I. Czekaj, O. Kroecher, G. Piazzesi, J. Mol. Catal. A: Chem. 280 (2008) 68.
[67] D. Nicosia, I. Czekaj, O. Krocher, Appl. Catal. B 77 (2008) 228.

[68] M. Wallin, H. Gronbeck, S.A. Lloyd, M. Skoglundh, Appl. Surf. Sci. 235 (2004) 487.
[69] C.W. Bauschlicher Jr., Chem. Phys. Lett. 246 (1995) 40.
[70] P.J. Stephens, F.J. Devlin, C.F. Chabalowski, M.J. Frisch, J. Phys. Chem. 98 (1994) 11623.
[71] P. Carbonniere, V. Barone, Chem. Phys. Lett. 399 (2004) 226.
[72] A.D. Becke, Phys. Rev. A 38 (1988) 3098.
[73] A.D. Becke, J. Chem. Phys. 98 (1993) 5648.
[74] S.H. Vosko, L. Wilk, M. Nusair, Can. J. Phys. 58 (1980) 1200.
[75] C. Lee, W. Yang, R.G. Parr, Phys. Rev. B: Condens. Matter Mater. Phys. 37 (1988) 785.
[76] C.E. Ruggiero, S.M. Carrier, W.E. Antholine, J.W. Whittaker, C.J. Cramer, W.B. Tolman, J. Am. Chem. Soc. 115 (1993) 11285.
[77] C. Lamberti, S. Bordiga, M. Salvalaggio, G. Spoto, A. Zecchina, F. Geobaldo, G. Vlaic, M. Bellatreccia, J. Phys. Chem. B 101 (1997) 344.
[78] M. Radoń, E. Broclawik, J. Phys. Chem. A 115 (2011) 11761.
[79] A.W. Aylor, S.C. Larsen, J.A. Reimer, A.T. Bell, J. Catal. 157 (1995) 592.
[80] M. Tortorelli, K. Chakarova, L. Lisi, K. Hadjiivanov, J. Catal. 309 (2014) 376.
[81] S.A. Bates, A.A. Verma, C. Paolucci, A.A. Parekh, T. Anggara, A. Yezerets, W.F. Schneider, J.T. Miller, W.N. Delgass, F.H. Ribeiro, J. Catal. 312 (2014) 87.
[82] Y.H. Yeom, J. Henao, M.J. Li, W.M.H. Sachtler, E. Weitz, J. Catal. 231 (2005) 181.